

An Analysis of the Low-Frequency Current Fluctuations in the Strait of Georgia, from June 1984 until January 1985

MICHAEL W. STACEY, STEPHEN POND AND PAUL H. LEBLOND

Department of Oceanography, University of British Columbia, Vancouver, B.C. V6T 1W5, Canada

HOWARD J. FREELAND AND DAVID M. FARMER

Institute of Ocean Sciences, Sidney, B.C. V8L 4B2, Canada

(Manuscript received 7 April 1986, in final form 12 September 1986)

ABSTRACT

A description of the low-frequency (≈ 10 to 30 days period) current fluctuations in the Strait of Georgia is presented. Velocity time series from four cyclesonde moorings and five current meter moorings, spanning the time interval from June 1984 until January 1985, are analyzed. Emphasis is placed on identifying the forcing mechanisms and determining the spatial structure of the low-frequency flow.

The nonlinear interaction of semidiurnal tidal constituents with bottom topography caused a near-bottom, low-frequency oscillation that was coherent over the span of the experimental array (≈ 11 km). The tides were important elsewhere in the water column too, and altogether directly accounted for 37% of the low-frequency energy in the Strait.

There is evidence of significant wind forcing. An empirical orthogonal function analysis of the vertical structure of the current fluctuations yields strong evidence for the existence of wind-forced Ekman spirals. Typically, the orthogonal modes that dominate the variance near the surface rotate clockwise with depth and are coherent with the wind.

Longitudinal and transverse velocity correlations imply that at some depths the low-frequency current fluctuations are consistent with horizontally nondivergent, isotropic flow. They also suggest horizontal scales of less than 8 km.

1. Introduction

The Strait of Georgia is an estuarine body of water located between Vancouver Island and the mainland of British Columbia. The estuarine circulation is caused primarily by freshwater runoff from the Fraser River which spreads as a plume, rarely more than 10 m thick, over the surface of the Strait. In addition, there are significant tidal currents, the main constituents being M_2 (12.42 h period) and K_1 (23.93 h period). The amplitude of the tidal currents is generally about 20 to 30 cm s^{-1} , except in constricted regions of the Strait where it can be much larger. Many other flow phenomena, such as internal waves, wind-forced flow, fronts and deepwater renewal occur in the Strait, and a comprehensive review is given by LeBlond (1983).

This paper is an analysis of the low-frequency (≈ 10 to 30 days period) currents in the Strait of Georgia. It is known that these currents are as energetic as those caused by the diurnal and semidiurnal tides (Chang et al., 1976), but it has not been clear how these currents are being forced. They have not been found to be coherent with temperature, river runoff, sea level variations or air pressure (Chang et al., 1976), and they are sometimes coherent with the wind (Helbig, 1978; Schumacher et al., 1978) and sometimes not (Chang

et al., 1976). Also, simple models of bottom trapped topographic waves (Helbig and Mysak, 1976), and Kelvin waves (Yao et al., 1982) have not adequately simulated the observations. The motions are of small spatial scale relative to their frequency, certainly less than 40 km and likely less than 10 km (Chang et al., 1976; Schott and Mysak, 1980; Yao et al., 1985), and at times a simple model of baroclinic instability (Yao et al., 1985) predicts space and time scales similar to those observed. However, there are often significant discrepancies.

In an effort to understand the forcing mechanisms, and the spatial structure of the low-frequency currents, an array of four cyclesonde moorings and five current meter moorings was deployed in the southern part of the Strait for approximately seven months. In this paper, observational evidence for two forcing mechanisms, the wind and the tides, is presented. Also, the spatial structure of the flow is examined by calculating longitudinal and transverse velocity correlations.

2. The data

Figure 1 shows where the instruments were deployed in the Strait. Stations 1 to 4 were cyclesonde moorings

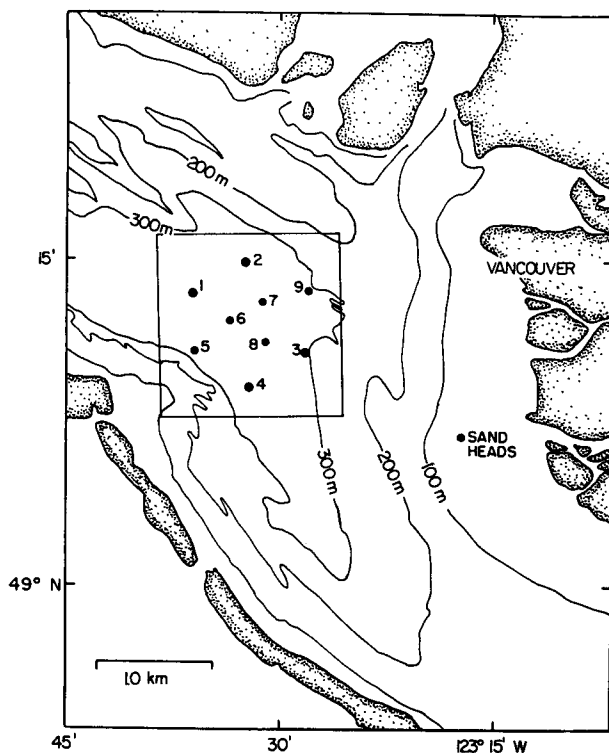


FIG. 1. Plan view of the Strait of Georgia in the vicinity of the study region (box). The cyclesonde moorings are stations 1 to 4, and the current meter moorings are station 5 to 9. The anemometer station was located at Sand Heads.

(current meters were also deployed at stations 2 and 4 part of the time; see Fig. 2), and stations 5 to 9 were current meter moorings. Figure 2 gives the details of the deployment for each station. At the current meter moorings, Aanderaa current meters sampling at 20 min intervals were located at 100, 200 and 290 m. The cyclesondes were set to profile to within 20 m of the surface and to a depth of 300 m.

Typically, a cyclesonde profile was obtained at least every six hours. Each velocity profile was vector averaged over about 20 m intervals and then interpolated to construct time series of velocity at the discrete depths of 40, 60, . . . , 280 m. (Velocity time series at 20 and 300 m were constructed from the velocity measurements obtained while the cyclesonde was resting at the top and bottom of its profiling range. Typically, this depth was within 5 m of 20 or 300 m.) The temperature and salinity measurements from each cyclesonde were processed in the same manner, except that they were not initially averaged over 20 m intervals. Following Yao et al. (1982, 1985), the time series were low-pass filtered by applying a running mean of 25 h three times successively. The time series were then resampled at 6 h intervals. This simple filter is used because the raw cyclesonde time series have data unequally spaced in time. For consistency, the same filter was applied to

the current meter data, and to the wind data obtained from Sand Heads (Fig. 1). For all of the time series, this filter reduces the amplitudes of the diurnal and semidiurnal tides to less than 1% of their original values, and passes 90% or more of the desired signal (≈ 10 to 30 days period).

Figure 3 shows filtered stick plots of the wind at Sand Heads and the currents at stations 1 and 3. Station 1 is fairly representative of the other stations, except station 3 which has anomalously large currents near the bottom. We see that the predominant wind direction is along the axis of the Strait. Also, there appears to be some obvious periodicity in the currents, particularly near the bottom of the Strait at station 3 (Fig. 3c). This and other characteristics of the flow will be discussed in the following sections.

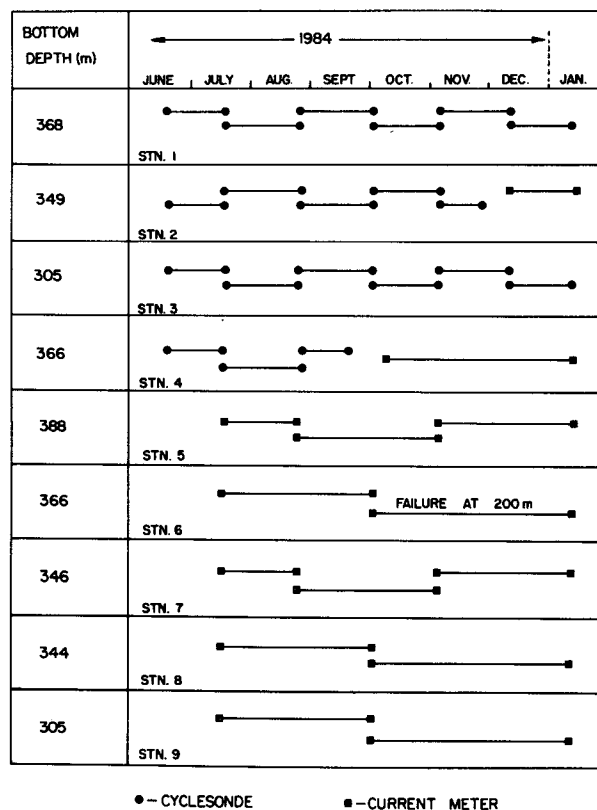


FIG. 2. The deployment details. The cyclesondes profiled to within 20 m of the surface and to a depth of 300 m. Current meters were placed at 100, 200 and 290 m. The current meter at 200 m at station 6 failed at the beginning of the second deployment. The successive time series of the velocity components from each cyclesonde and current meter mooring were patched by linearly interpolating from the end of one series to the beginning of the next. The endpoints of the interpolation where 24 h averages of U (east-west velocity) and V (north-south velocity). The lengthened time series were then filtered. When comparisons between stations were desired at 100, 200 or 280/290 m, the current meter data at station 4 was patched to the preceding cyclesonde data before filtering. The scalar time series were patched and filtered in the same way.

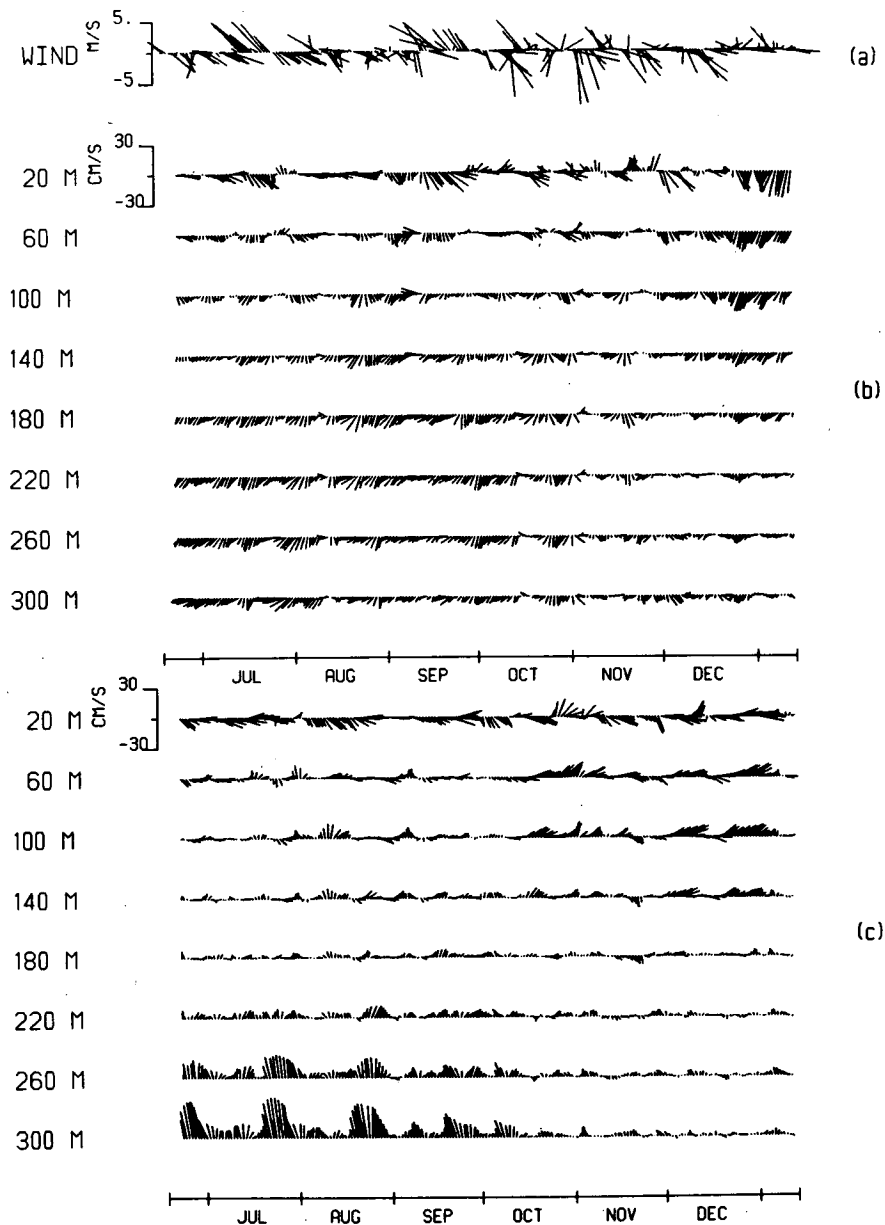


FIG. 3. Stick plots of (a) filtered winds at Sand Heads, (b) filtered currents at station 1, and (c) filtered currents at station 3. Every second depth is shown for the currents, and the data are plotted at daily intervals. The northward direction is vertically upwards on the page.

3. Means and variances

Figure 4 shows the mean velocity at four different depths. Near the surface (Fig. 4a), there is a net south-eastward drift approximately along the axis of the Strait of about 10 cm s^{-1} , consistent with the previous measurements of Chang et al. (1976) and Yao et al. (1985) which tended also to indicate a net eastwards flow. At middepth (Fig. 4b, c), the mean circulation is less intense and shows signs of becoming an anticlockwise gyre. Near the bottom (Fig. 4d), the mean circulation

is also anticlockwise, and tends to be more constrained by the bottom contours. The mean flow at some stations (station 4, and possibly stations 5 and 6) remains fairly unidirectional with depth while at other stations (station 3 in particular) it goes through a substantial change in direction.

Figure 5 shows the principal axes of the covariance matrices at the same depths. Stations 1 and 4 have noticeably the largest variance near the surface (Fig. 5a) and their major axes are directed almost along the axis of the Strait, the predominant wind direction. Sta-

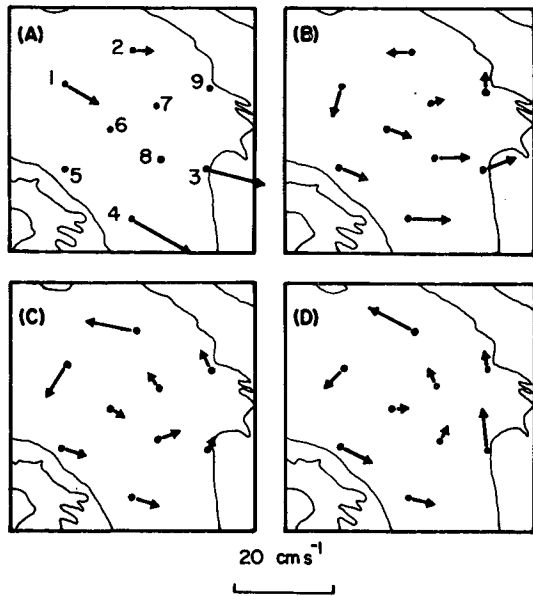


FIG. 4. Mean velocity vectors at (a) 20 m, (b) 100 m, (c) 200 m and (d) 290 m for the current meters and 300 m for the cyclesondes.

tions 2 and 3 have less variance, and at station 3 the variance appears to be almost isotropic. At 100 m (Fig. 5b), the variance is reduced, and at 200 m (Fig. 5c) it is further reduced, with the principal axes beginning to align along the bottom contours. Near the bottom (Fig. 5d), the variance is noticeably directed along the bottom contours, and at station 3 (one of the shallowest stations) there has been a dramatic increase in the variance, which is easily seen in the stick plots in Fig. 3c. It is possible that the same bottom-intensified flow occurred at some other stations, but was not noticed because it occurred at depths greater than the 290 to 300 m to which measurements were made. The stick plots in Fig. 3 also show that the bottom-intensified flow occurred primarily during the first third to one half of the measurement period.

Figure 6 shows the total kinetic energy (variance/2) as a function of depth. The data of Chang et al. (1976) have been included for comparison, and we see that their values are similar to those obtained here. Note the tendency for the variance to be surface intensified. Also, note that near the bottom there is a tremendous amount of variability in the variance. Station 3 has an order of magnitude more kinetic energy than station 6. It should again be pointed out, however, that the bottom intensification observed at station 3 may have occurred below the measuring devices at some other stations, although it does not occur near the bottom at station 9 which is just as shallow as station 3.

4. Autospectra

We know that the diurnal and semidiurnal tides account for much of the variance at higher frequencies,

but it has not been clear what is forcing the low-frequency currents. Given that the low-frequency flow is of relatively large amplitude and has a small spatial scale, however, it is likely that nonlinearities are dynamically important. It is certainly possible that nonlinear interactions between the semidiurnal and/or diurnal tidal constituents feed energy to lower frequencies. For example, the beat frequency of the M_2 and S_2 tides (the MSf frequency) is 0.069 cpd which corresponds to a period of 14.77 days; a nonlinear interaction between M_2 and S_2 would feed energy into this frequency. Other possible frequencies are the beat frequency of the M_2 and N_2 ($T = 12.66$ h) tides (the M_m frequency) which has a period of 27.55 days, and the N_2 and S_2 tides which has a period of 9.61 days.

To check if the tides can account for much of the low-frequency energy, we examined raw spectral plots of the currents. The length of each data block was chosen to make MSf (and M_m when possible) a Fourier frequency. Figure 7 shows autospectra for stations 1 through 4. There has been no averaging over frequency, and no error estimates are given because the normal statistical estimates of error are based on normal distributions and do not apply to deterministic motions like the tides. We see immediately that there is a substantial low-frequency tidal signal at many locations in the Strait. Station 1 has a very noticeable MSf peak in both U and V near the surface and in V near the bottom; there are also peaks at M_m . Station 2 has tidal peaks in U and V near the bottom and V near the surface. At station 3, V near the bottom is almost entirely tidal and very large in amplitude. Station 4 has tidal peaks in U and V near the surface and bottom.

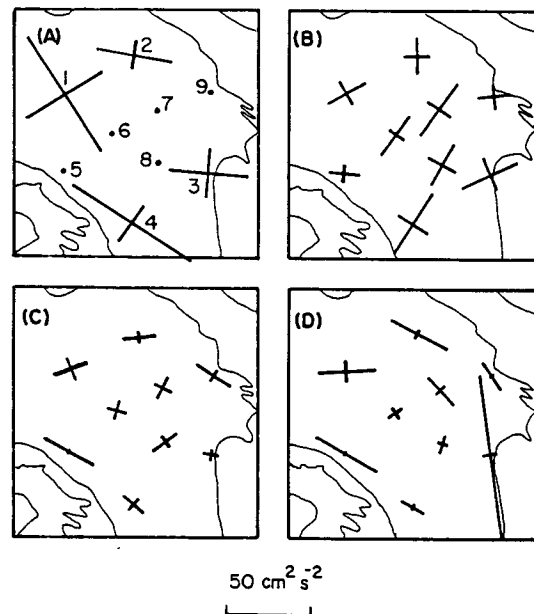


FIG. 5. Principal axes of the covariance matrices for the same depths as in Fig. 4.

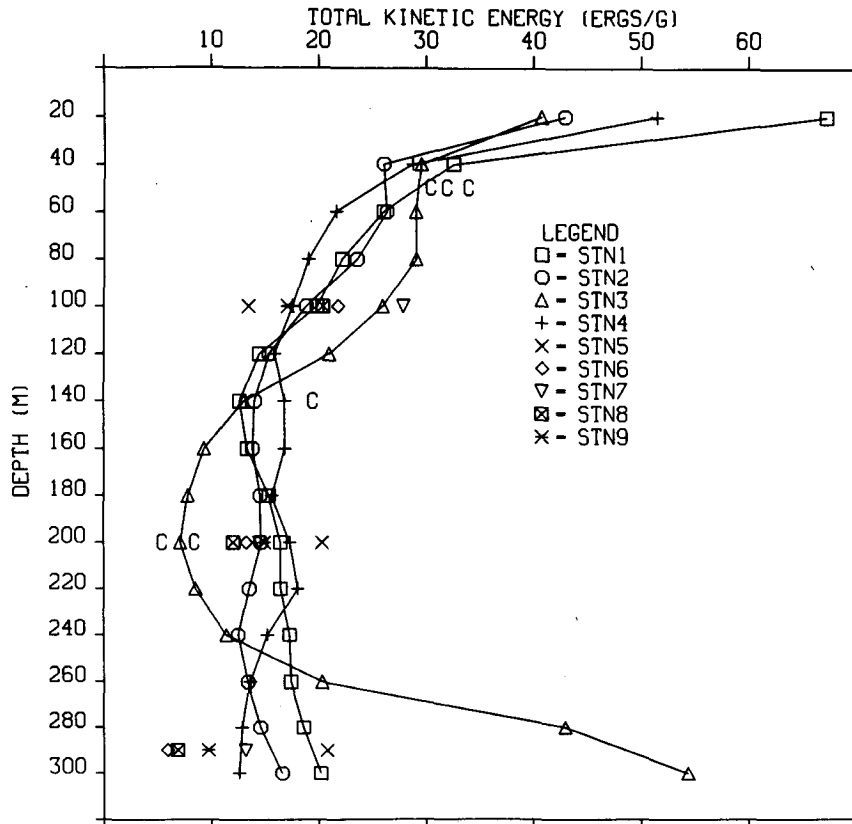


FIG. 6. Profiles of the total kinetic energy for all nine stations. Also included are the results of Chang et al. (1976), indicated by the letter C.

Tidal peaks were also evident in the autospectra for stations 5 through 9, and a reanalysis of the data used by Chang et al. (1976) and Yao et al. (1985) yielded a number of tidal peaks comparable in amplitude to those shown here. There is in fact evidence of an MSf peak in Fig. 7 of Chang et al. (1976). It seems therefore that the tides can likely account for much of the low-frequency energy much of the time.

5. Harmonic analysis

To estimate the fraction of the low-frequency energy explained by the tides, harmonic analysis (Foreman and Henry, 1979) was done on the time series of the current velocities. When doing this analysis, one cannot take into account doppler shifting of the constituent frequencies by the mean flow or changes in the amplitude of the constituents with time, but we still feel it yields a reasonable estimate of the importance of the tides in the Strait. Table 1 shows the tidal constituents that were fitted to each times series. Typically, the shorter a time series is, the fewer the number of constituents that can be fitted to it and, of those that are fitted to it, the farther apart they must be in frequency space. The number used for each station was found by trial and error. Whenever two constituents of similar

frequency were of almost the same amplitude and approximately 180° out of phase, at least one constituent was deleted and the calculation repeated.

The fraction of the variance was calculated as

$$F = 1 - \frac{S_r^2}{S_D^2} \tag{1}$$

where

$$S_r^2 = \left[\frac{\text{(sum of the square of the residuals)}}{[N - (2M - 1)]} \right]$$

S_D^2 variance of the time series, with the mean removed

M number of constituents, including the offset Z_0 (see Table 1)

N number of data points.

Figure 8 shows profiles of F for stations 1 through 4, and Table 2 lists F for stations 5 through 9. Typically, about one third of the variance can be explained by the tides. In fact, for the whole array and at all depths, $F = 0.37$. The general conclusion is that the tides likely account for a significant percentage of the low-frequency energy in the Strait, and at some locations are probably at times the dominant contribution. Note also that the tides can vary significantly in importance from

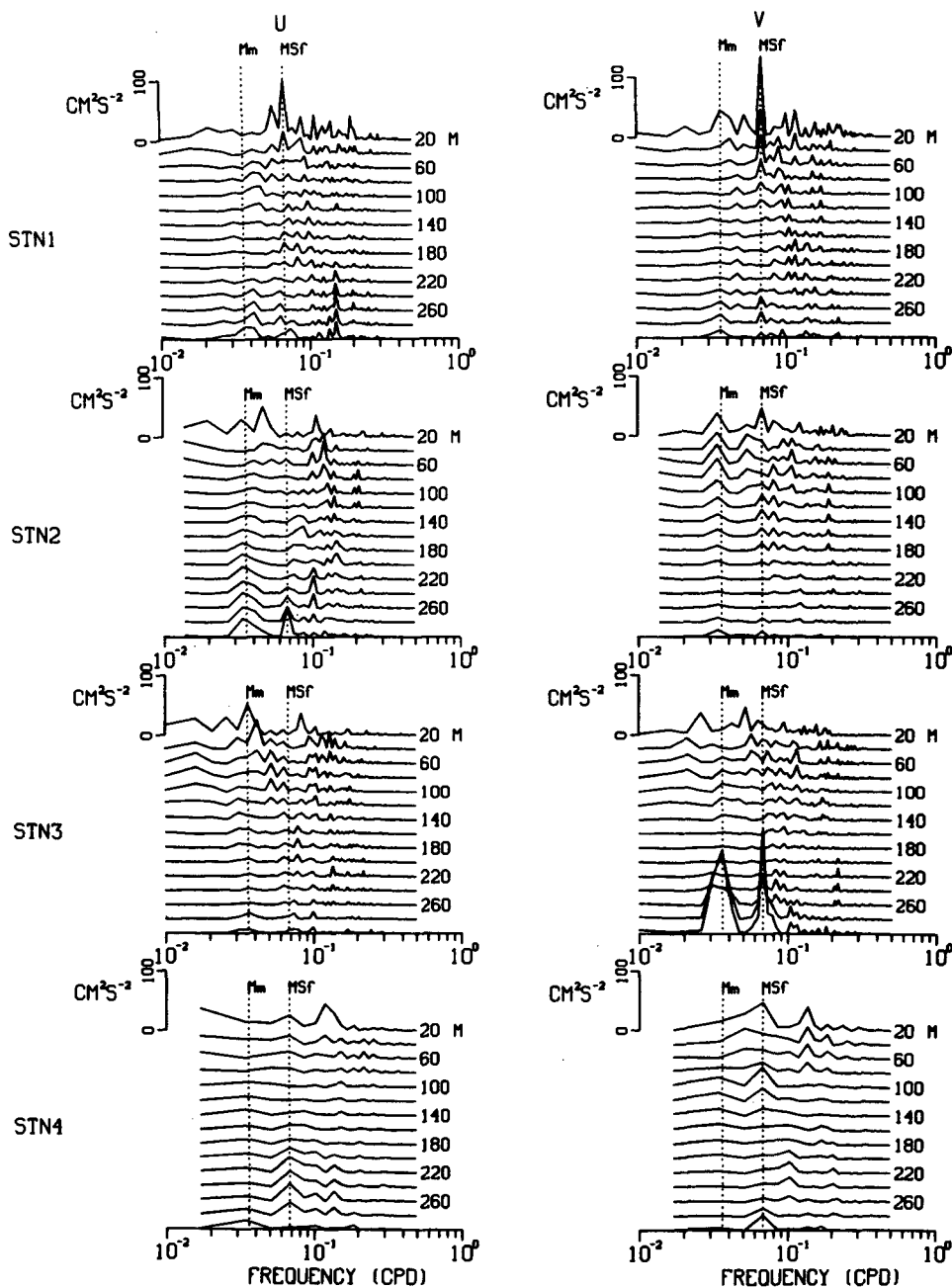


FIG. 7. Autospetra of U and V for stations 1 through 4, at 20 m intervals. For stations 1 and 3, the length of each data block is 13 MSf cycles, which corresponds to approximately 7 M_m cycles. For stations 2 and 4, the length of each data block is ten and four MSf cycles respectively. There has been no averaging over frequency. The dotted vertical lines indicate the M_m and MSf frequencies.

place to place. Near the surface at station 2 for example, U is about 20% tidal; the same applies to U at station 1 between 60 and 100 m, V at station 3 above about 180 m, V at station 6 at 20 and 290 m, and V at station 9 at 100 m. Near the bottom at station 3, on the other hand, V is about 60% tidal. If only data from the beginning of the time series until the end of September at station 3 is analyzed (Fig. 3c), we find that V is about

90% tidal, which implies that the anomalously large currents at station 3 are tidal in origin.

6. Cross-spectra

Cross-spectra were calculated in order to determine the horizontal and vertical distances over which the low-frequency currents were coherent. Results similar

TABLE 1. Tidal constituents used in the harmonic analysis. Crosses indicate the constituents that were used at each station.

Tide	Period (days)	Station								
		1	2	3	4	5	6*	7	8	9
Z_0	∞	X	X	X	X	X	X	X	X	X
Ssa	182.62	X	X	X		X	X	X	X	X
MSm	31.81	X	X	X		X	X	X	X	X
M_m	27.55	X	X	X	X	X	X	X	X	X
MSf	14.77	X	X	X	X	X	X	X	X	X
Mf	13.66	X	X	X	X	X	X	X	X	X

* At 200 m, Ssa, and MSm were not used.

to those of Chang et al. (1976) and Yao et al. (1982) were obtained, but there were also some significant differences.

Matrices of the U and V coherence, similar to those computed by Yao et al. (1982), are shown in Fig. 9 for the 4 cyclesonde stations. Chang et al. and Yao et al. found the currents between 50 and 200 m not to be significantly coherent. Here, V at station 2 is coherent over almost the entire measurement range in the 14 to 148 day frequency band (lowest frequency band). Also,

TABLE 2. Fraction of the low-frequency variance explained by the tides at the current meter stations.

Station	Depth (m)	U	V
5	100	0.34	0.23
	200	0.63	0.55
	290	0.55	0.51
6	100	0.32	0.36
	200	0.34	0.16
	290	0.24	0.14
7	100	0.31	0.35
	200	0.38	0.43
	290	0.59	0.42
8	100	0.30	0.33
	200	0.47	0.47
	290	0.38	0.39
9	100	0.30	0.18
	200	0.41	0.53
	290	0.45	0.54

note that U at 20 and 220 m at station 1 is coherent in the 7 to 14 day frequency band, and V at 100 and 300 m at station 3 is coherent in the lowest frequency band. In both of these cases, the phase difference between the depths is close to 180° . A number of these properties of the flow are reflected in the empirical orthogonal functions described in section 8b.

Perhaps the most interesting results are those involving cross-spectra of velocity components from the same depth but different stations. The deepest currents showed a high level of coherence in the lowest frequency band. The results are tabulated in Table 3. We see that almost all of the stations are coherent with each other and that the phases are frequently either approximately 0° or 180° . Notable exceptions are U and V at station 6 and V at station 4, which have poor coherence with the other velocity components. Also, V at station 1 was never close to 0° or 180° out of phase with other components. In spite of these few exceptions it is obvious that during the period of observation, a low-frequency oscillation, coherent over the span of the experimental array, occurred near the bottom of the Strait. The coherences could be quite large between velocity components. For example, U at station 1 and V at station 3 had a coherence of 0.8 when 10 frequency bands were averaged, i.e., when the 95% significance level was 0.28. We also point out, however, that when the currents are compared using only that portion of each time series that does not include the anomalously large currents at station 3 (Fig. 3c), i.e., when approximately the last half of each time series is used, the coherences tend to decrease, so the deep coherent motion may not always be present.

The coherent motion illustrated in Table 3 can be interpreted in terms of empirical orthogonal functions (section 8a). First, however, we will show how the coherences in Table 3 are related to the phase of the MSf tide.

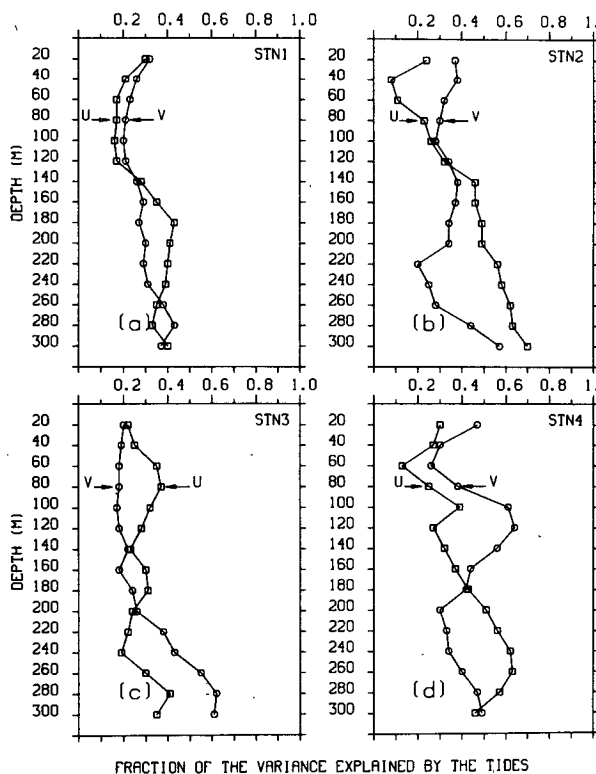


FIG. 8. Fraction of the variance explained by the tides as a function of depth for (a) station 1, (b) station 2, (c) station 3 and (d) station 4.

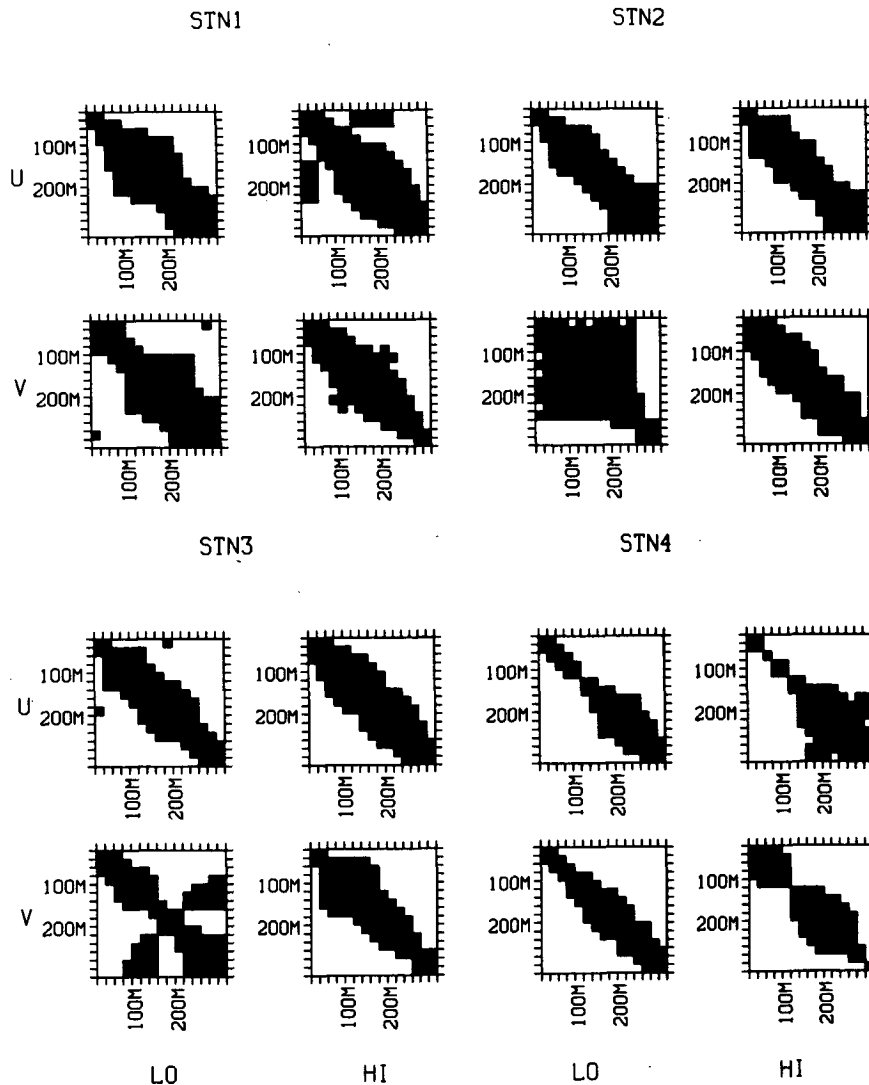


FIG. 9. Matrices of U and V coherence for each depth pair for stations 1 through 4. Blackened squares signify depth pairs that are significantly coherent. For stations 1, 2 and 3, the low frequency (LO) corresponds to the 14 to 148 day band, and the high frequency (HI) to the 7 to 14 day band. For station 4, the bands are 13 to 59 days, and 7 to 13 days. The 95% significance level is 0.28 for stations 1, 2 and 3, and 0.63 for station 4.

7. The MSf tide

The lowest frequency band contains the MSf tide (and other low-frequency tidal constituents), and the harmonic analysis showed that much of the variance near the bottom can be accounted for by the tides. Here, we show that the phase of the MSf tide near the bottom mirrors the phases of the coherence.

Table 4 shows the phase of each MSf velocity component at the deepest depth at each station relative to the phase of the V component at station 3. The phase was calculated simply by Fourier transforming at each station data blocks covering the same time interval. The length of each data block was chosen to be ten

MSf cycles which is also the length of each data block used to compute the values in Table 3. Inspection of Tables 3 and 4 shows that the phase differences between the coherent velocity components are reflected in the phases of the MSf tide. Between the coherent stations, the MSf tide tends to be either approximately in phase or 180° out of phase. This result suggests that the low-frequency oscillation near the bottom of the Strait was tidally forced.

The change in phase of the MSf tide with depth was determined at each cyclesonde station, but only at station 4 was a clear relationship found. (Because of the short length of the cyclesonde record at station 4 (Fig. 2), the data block in this case was only four MSf cycles

TABLE 3. Phases between the deepest coherent currents at each station in the lowest frequency band (14 to 148 days period). When two velocity components are significantly coherent, the phase is listed; otherwise, a cross is inserted. The terms U_i and V_i signify the east-west and north-south velocity components respectively at the i th station. The term U_iU_j , for example, signifies the coherence between the U velocity components at the i th and j th stations. As used below, $i = \text{row}$ and $j = \text{column}$. The numbers listed along the outside of each box designate the station numbers that each row or column corresponds to. The 95% significance level is 0.28.

U_iU_j (above diagonal), V_iV_j (below diagonal)										U_iV_j									
Row	1	2	3	4	5	6	7	8	9	Row	1	2	3	4	5	6	7	8	9
1		-1	-25	-174	-176	X	-6	X	8	1	X	180	163	-19	5	X	176	167	176
2	X		-23	-173	-160	X	-4	-63	4	2	X	-179	164	-25	18	X	-179	-179	175
3	-88	18		-123	-114	X	30	-39	61	3	98	-163	-174	X	60	X	-128	X	-128
4	X	X	-174		11	X	171	91	-169	4	X	X	-22	X	-175	X	2	1	-2
5	61	X	154	X		X	152	57	173	5	-109	-19	-32	125	178	X	-5	1	11
6	X	X	X	X	X		30	-12	58	6	X	X	-139	36	X	X	X	X	X
7	-114	-4	-22	X	-179	X		-66	17	7	X	X	177	6	20	X	-167	-178	-170
8	-117	X	-17	X	-180	X	-1		85	8	X	X	-107	56	111	X	-64	X	-82
9	-99	6	-13	X	-173	X	6	1		9	X	172	158	-20	0	171	X	-169	X

long.) The U component had almost constant phase from 20 to 100 m, changed phase by 180° between 100 and 140 m, and then had almost constant phase again down to 300 m. The change in amplitude with depth is shown in the autospectra for U at station 4 (Fig. 7). This is a simple mode 1 response, so it seems that at least some of the time a low-frequency internal tide can be set up in the Strait. It is also likely, however, that nonlinearities often cause considerable distortion of the simple response.

8. Empirical orthogonal functions

a. Horizontal

The picture that is developing of a coherent, near-bottom current fluctuation is enhanced by an examination of the empirical orthogonal functions (EOFs) at depth. (See Kundu and Allen, 1976, for example, for a description of EOFs.) Using velocity time series (with the mean removed) from 280 m at the cyclesonde stations (280/290 m at station 4) and from 290 m at the current meter stations, complex, i.e., two-dimensional, EOFs were calculated using the largest common record length.

TABLE 4. Phase of MSf tide at the deepest depth relative to the phase of V at station 3. The phase is the amount in degrees by which V at station 3 lags the other velocity component.

Station	U	V
1	181	66
2	165	16
3	189	0
4	-14	149
5	-43	157
6	171	-79
7	172	-3
8	-144	-12
9	127	-37

Table 5a lists the variance explained by the first three modes at each station. The first mode explains 65% of the total variance. At station 3, it explains almost 90% of the variance, and it is the dominant mode at all stations except station 6. Recall that station 6 was not well correlated with the other stations (section 6). Figure 10 shows the first mode eigenfunction. The directions, which are arbitrary to within a constant angle of rotation, were fixed by making the arrow at station 3 lie along the principal axis of the covariance matrix (see Fig. 5). We see that a low-frequency oscillation, tending to move along bottom contours, occurred near the bottom of the Strait. When the motion was southwards on the eastern side of the Strait, it was northwards on the western side, and vice versa. Autospectra of the real and imaginary, time-dependent parts of the first mode show it to have dominant peaks at the beat frequencies of the M_2 , S_2 and N_2 tides, i.e., 0.036, 0.068 and 0.104 cpd, so it can be considered a tidal mode. Such a result is to be expected because the first mode explains almost 90% of the variance at tidally dominated station 3. Also,

TABLE 5a. Fraction of the variance explained by the first three horizontal modes at each station at 280/290 m, and fraction of total variance explained by each mode.

Station	Mode		
	1	2	3
1	0.40	0.16	0.39
2	0.74	0.00	0.00
3	0.89	0.07	0.02
4	0.46	0.09	0.06
5	0.52	0.35	0.04
6	0.12	0.09	0.26
7	0.74	0.06	0.02
8	0.33	0.30	0.05
9	0.64	0.00	0.00
Fraction of total variance	0.65	0.12	0.08

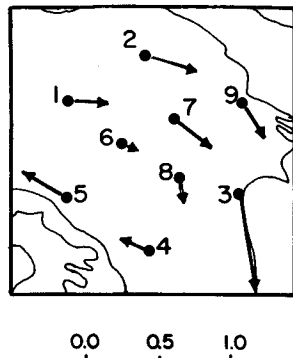


FIG. 10. The first mode empirical orthogonal function at 280/290 m. Its direction has been fixed by making the arrow at station 3 lie along the major axis of the covariance matrix. The scale below the figure determines the magnitude of each component of the eigenfunction. The eigenfunction has been normalized so that its modulus is equal to one.

inspection of Table 4 shows that the motion of the first mode is similar to that of the MSf tide alone.

Horizontal EOFs can also be calculated from the nine velocity time series at 100 and 200 m, but it turns out that vertical EOFs, calculated at the four cyclesonde stations, shed more light on the currents at shallower depths.

b. Vertical

Using cyclesonde data, Yao et al. (1985) interpreted the vertical structure of the *V* component velocity fluctua-

tions in terms of one-dimensional EOFs. Applying the same calculation to the four cyclesonde stations described here, we obtained results that were quite similar to Yao et al. As Yao et al. found, the upper and lower parts of the water column were dominated by different modes, the first mode usually dominating in the upper half and the second or third in the lower. There was an exception, however. At station 4, the second mode dominated in the upper 60 m, the first mode from 60 to 220 m, the first and third modes from 220 to 260 m, and the fourth mode from 260 to 300 m. It is possible that Yao et al. did not observe this type of behavior because their measurements did not go above 60 m, and therefore could not record any response above that depth. When the EOFs were re-calculated at station 4 using 60 m as the shallowest depth, the second mode mentioned above disappeared, the third mode became the second mode, and the fourth mode became the third mode. In other words, the EOFs became similar to those at the other stations.

Instead of considering just the *V* component of velocity, it is more general to consider *U* and *V* together using complex EOFs. Figures 11 through 14 show the first three or four modes (the fourth mode is shown only if it dominates the variance at some depth) as a function of depth for the four cyclesonde stations, and Fig. 15 shows the fraction of the variance explained by each mode at each station as a function of depth. Table 5b lists the fraction of the total variance explained by each mode. Each mode can be rotated by an arbitrary angle, and here the arrow at 300 m has been arbitrarily chosen to point vertically on the page.

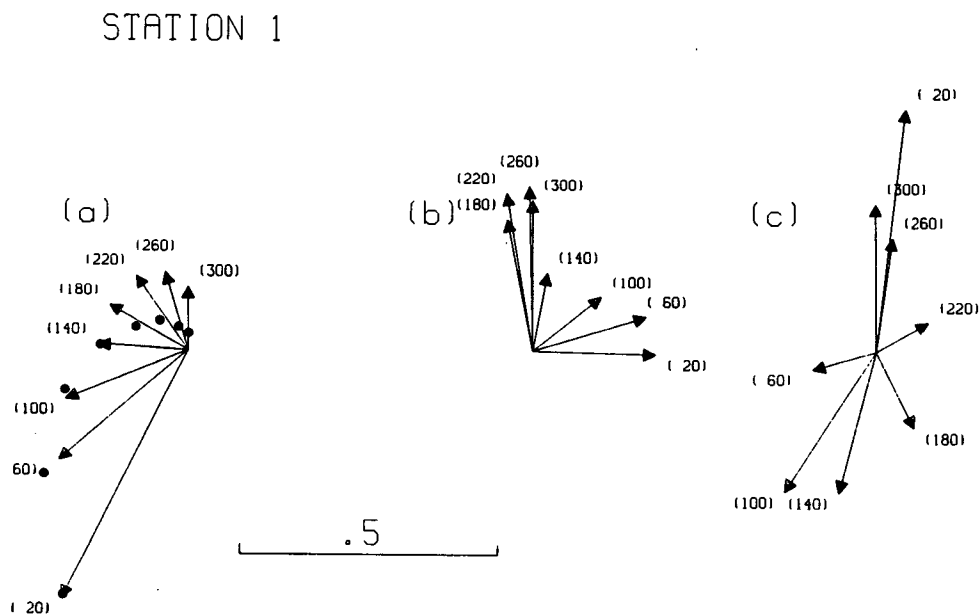


FIG. 11. The first (a), second (b) and third (c) orthogonal modes at station 1, plotted at every second depth, i.e., at 40 m intervals. Each mode has been arbitrarily picked to point vertically on the page at 300 m. The dots in (a) locate the tips of the velocity vectors of the classical Ekman spiral described in the text.

STATION 2

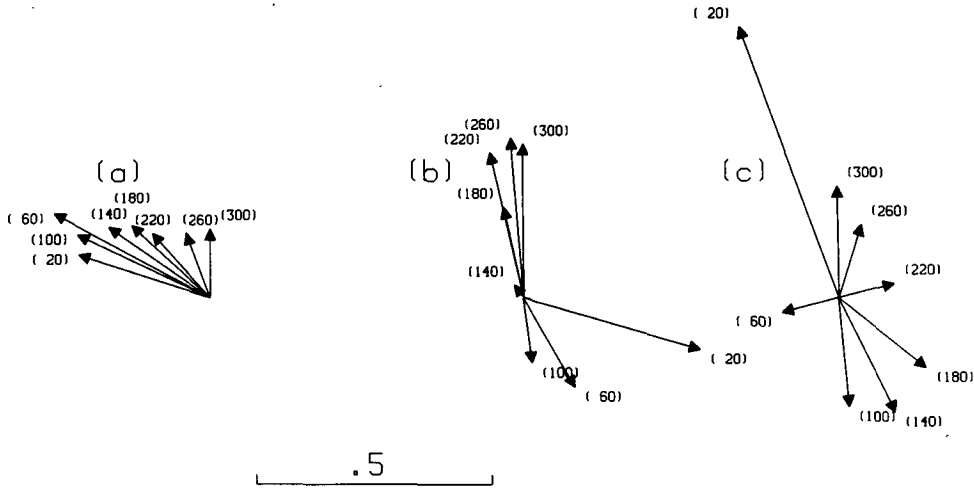


FIG. 12. The first (a), second (b) and third (c) orthogonal modes at station 2, plotted at every second depth. Each mode has been arbitrarily picked to point vertically on the page at 300 m.

At station 1, the first mode (Fig. 11a) rotates clockwise with depth from 20 to 300 m and looks very much like an Ekman spiral. It dominates the variance to a

depth of 140 m. In the lower portion of the water column, the second mode dominates and tends to be more unidirectional (Fig. 11b). The third mode (Fig. 11c)

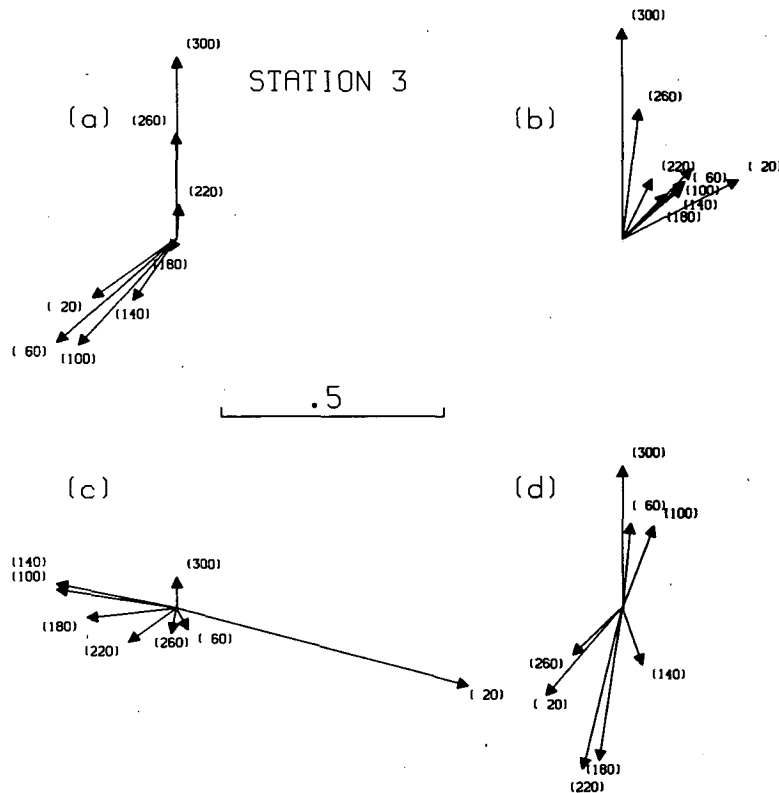


FIG. 13. As in Fig. 12 but for the first (a), second (b), third (c) and fourth (d) orthogonal modes at station 3.

STATION 4

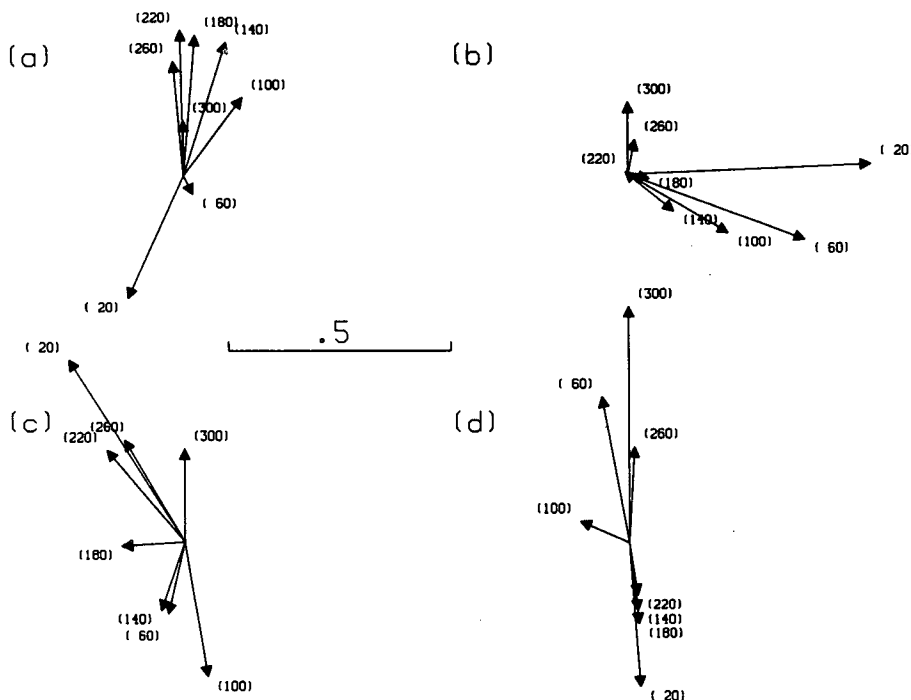


FIG. 14. As in Fig. 12 but for the first (a), second (b), third (c) and fourth (d) orthogonal modes at station 4.

exhibits a consistent anticlockwise rotation with depth and makes its most important contribution to the variance at 120 m.

At station 2, the first mode (Fig. 12a) rotates mostly clockwise with depth, and dominates the variance over much of the measurement range. This dominant first mode explains the *V* coherences obtained at station 2 (Fig. 9). Below 220 m, the second mode (Fig. 12b) dominates the variance and, like the corresponding second mode at station 1, tends to be unidirectional there. Above 140 m, it exhibits a clockwise rotation similar to that of the first mode at station 1. The third mode (Fig. 12c) exhibits a consistent anticlockwise rotation, similar to the behavior of the third mode at station 1, and contributes the largest fraction to the variance at 20 m.

At station 3, the first and second modes (Fig. 13a, b) contribute comparable variance near the bottom. Also, the first mode dominates between 40 and 140 m. The first mode in particular is unidirectional below 220 m, similar to the behavior of the bottom dominant modes at stations 1 and 2. The behavior of the first mode, which rotates by approximately 140° between 180 and 200 m, is reflected in the *V* coherences at station 3 (Fig. 9). The third mode (Fig. 13c) is most important at 20 m, and exhibits a clockwise rotation with depth down to 140 m. The fourth mode (Fig. 13d) is the most important between 180 and 200 m, and from 20 to 300 m rotates clockwise by more than 360°.

At station 4, the first mode (Fig. 14a) dominates over much of the measurement range below 100 m. This dominance is reflected in the *U* coherences at station 4 (Fig. 9). The second mode, which dominates from 20 to 100 m, rotates clockwise with depth like an Ekman spiral down to 140 m, similar to the behavior of the first mode at station 1 and the second mode at station 2. The third mode, although it explains more of the total variance than the fourth, is nowhere dominant, whereas the fourth mode dominates at 300 m.

At stations 1 and 4, as already mentioned, the modes that dominate the variance near the surface resemble Ekman spirals there. Note also that stations 1 and 4 have the most total variance near the surface (Fig. 6), and have principal axes directed approximately along the axis of the Strait (Fig. 5), the predominant wind direction (Fig. 3). (The winds are discussed in the next section.) This result suggests that the winds were having a significant influence on the currents at these two stations. In fact, a simple Ekman spiral (e.g., see Pond and Pickard, 1983), i.e.,

$$U = V_0 \cos\left(\frac{\pi}{4} + \frac{\pi z}{D_E}\right) \exp\left(\frac{\pi z}{D_E}\right)$$

$$U = V_0 \sin\left(\frac{\pi}{4} + \frac{\pi z}{D_E}\right) \exp\left(\frac{\pi z}{D_E}\right)$$

where *z* is zero at the surface and negative below, fits the first mode at station 1 remarkably well down to a

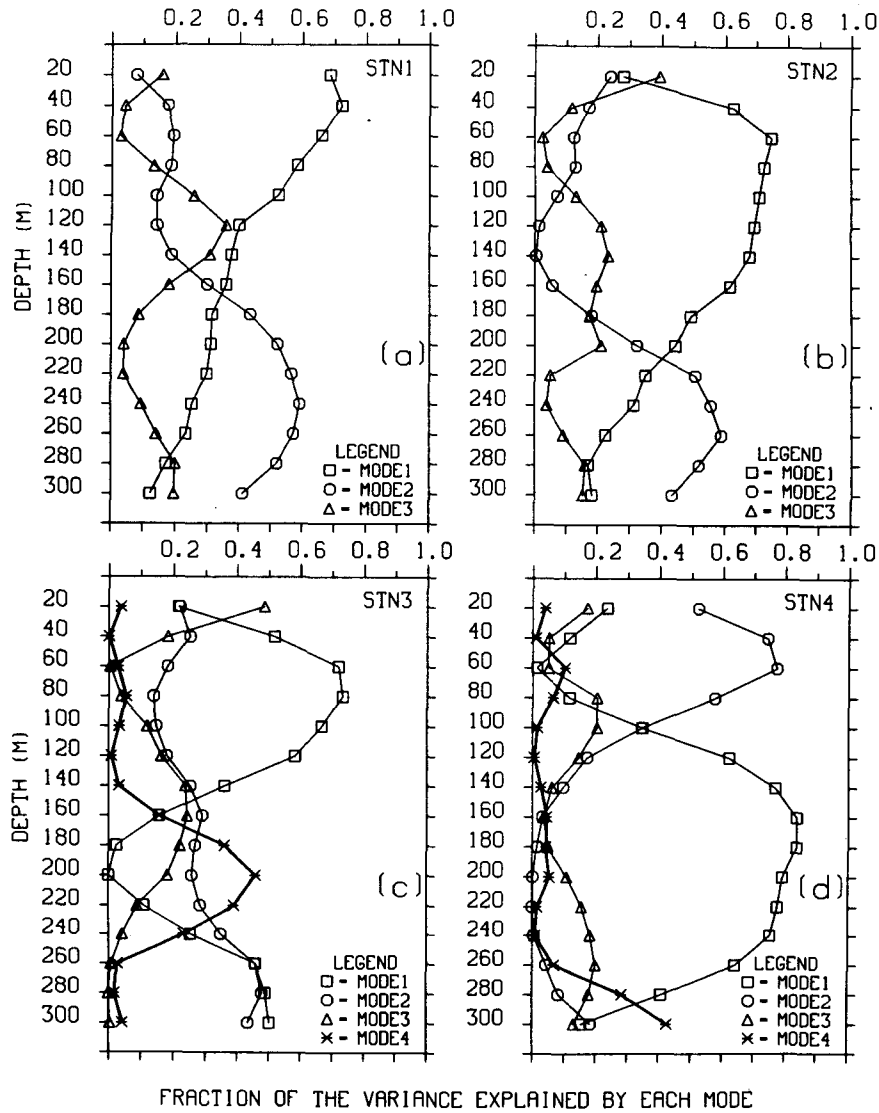


FIG. 15. Fraction of the variance explained by each mode as a function of depth at (a) station 1, (b) station 2, (c) station 3 and (d) station 4.

depth of 140 m (Fig. 11a), the depth to which it dominates the variance (Fig. 15). An Ekman depth D_E of 325 m was used and V_0 was set equal to 0.66 in non-dimensional units, which corresponds to an amplitude

of about 10 cm s^{-1} at 20 m. The Ekman depth is quite large, but possibly turbulence induced by the tides increases the depth to which the wind forced momentum can diffuse. This mode is discussed in more detail by Stacey et al. (1986).

TABLE 5b. Fraction of the total variance explained by the first four vertical modes at the four cyclesonde stations.

Station	Mode			
	1	2	3	4
1	0.47	0.28	0.14	0.06
2	0.49	0.24	0.16	0.06
3	0.47	0.30	0.12	0.07
4	0.44	0.31	0.13	0.06

Rotary cross-spectra (Moore, 1973) show that the first mode at station 1 is coherent at low frequencies with the second mode at station 4. In addition, it is also coherent with the second and third modes at station 2, the second, third and fourth modes at station 3, and the first mode at station 4. Near the surface, all of these modes exhibit at least some clockwise rotation with depth, except the third mode at station 2 and the second mode at station 3. Stations 2 and 3 have the least total variance near the surface (Fig. 6), so perhaps it is not surprising that the clockwise rotation expected

for wind forced currents is not always found there. Stations 2 and 3 are closer to the mouth of the Fraser River than stations 1 and 4, and so possibly the wind there was to a greater extent insulated by fresh water runoff from the bulk of the water column. Also, the third mode at station 2 dominates at only one depth, so the sense of its rotation may not be dynamically important.

A number of the modes that are coherent with the first mode at station 1 contribute considerable variance at depths greater than 160 m. For example, the second mode at station 3 accounts for approximately 50% of the variance at 300 m. At station 3 at 300 m, harmonic analysis (section 5) showed the tides to account for about 60% of the variance in the north-south direction, 90% when only the anomalously large currents are analyzed. That is, the first mode at station 1, which might be classified as a wind-generated mode, is coherent with the second mode at station 3, which has significant tidal energy. Also, autospectra of the clockwise rotating modes show significant peaks at tidal frequencies. Even the first mode at station 1, which exhibits behavior very similar to an Ekman spiral, has substantial energy at tidal frequencies. Harmonic analysis suggests that as much as 30% of its energy is tidal in origin. As already mentioned, possibly it is the tides that cause the first mode to have such a large Ekman depth. These results suggest that nonlinear interactions between the wind and tidally forced motions caused these motions to become modified in a way that made them coherent.

We have seen that, contrary to the modes that dominate near the surface, the modes that dominate at depth tend at depth to be relatively unidirectional. They are also coherent with each other, the only exception being the second modes at stations 1 and 3, which are not coherent, even though U at station 1 and V at station 3 are highly coherent (section 6). This coherence between U and V is reflected entirely in the coherence of the second mode at station 1 with the first mode at station 3.

Station 4 is different from the other stations in that the fourth mode becomes very important at 300 m. The reason for this result is not known, but possibly the cyclesonde at station 4 did not profile deep enough to record fully the deep, coherent motion. When empirical orthogonal functions are calculated at station 2 using 220 m as the maximum depth, a result similar to that found at station 4 is obtained. Modes 1 and 2 each explain less of the variance at 220 m than mode 3, which dominates only at that depth.

9. Winds

Rotary cross-spectra show that the four leading modes at each cyclesonde station are all coherent with the wind, except for the second modes at stations 2 and 3 and the third and fourth modes at station 4.

At station 1, recall that the first mode resembles very closely an Ekman spiral (Fig. 11a) and dominates the variance near the surface (Fig. 15). Its maximum coherence with the winds is 0.65 (the 95% significance level is 0.28) at -0.09 cpd.¹ In fact it is coherent with the winds over a broad range of frequencies; from -0.15 to -0.06 cpd, and at 0.03 cpd. This result strongly suggests that the first mode was to a large extent forced by the wind, although, as already discussed in the previous section, it has energy at tidal frequencies. This tidal energy is not, of course, coherent with the wind. The second mode, which dominates at depth (Fig. 15), is coherent with the wind in only one frequency band; a coherence of 0.36 at -0.04 cpd. The third mode is highly coherent with the wind and has a maximum coherence of 0.52 at 0.05 cpd.

Quite a different result is obtained at station 2. The first mode, which dominates the variance over much of the measurement range, is most coherent with the wind in a significantly higher frequency band, not at the lower frequencies where most of the variance is found. It has a maximum coherence of about 0.46 at -0.17 cpd. The second mode, which dominates at depth, is not coherent with the wind and the third is only nominally coherent at about -0.14 cpd.

At station 3, the first mode is coherent with the wind at low frequencies at about the 0.3 level, but the third mode, which dominates near the surface, is very coherent with the wind. It has a maximum coherence of 0.62 at -0.09 cpd and is coherent with the wind at frequencies ranging from -0.14 to -0.06 cpd. This behavior suggests that the third mode was a wind forced mode. The fourth mode, which dominates the variance only from 180 to 200 m, is coherent at about the 0.35 level at all negative frequencies greater than -0.06 cpd. The fourth mode is similarly coherent with the wind at 0.17 to 0.2 cpd.

At station 4, the first mode, which dominates at depth, is more coherent with the wind than the second mode, which dominates near the surface and resembles an Ekman spiral there. The first mode has a coherence of about 0.5 at -0.1 cpd, while the second mode has a coherence of about 0.3 at 0.1 cpd. This somewhat curious result is probably caused by the short length of the cyclesonde time series at station 4. When a shortened time series is used at station 1, similar anomalous results are obtained.

The results presented here are very different from those of Chang et al. (1976), who, at similar locations in the Strait, found poor coherence with the wind. However, calculations of the low-frequency kinetic en-

¹ Negative (positive) frequencies refer to the clockwise (anticlockwise) rotating components of each vector series (Mooers, 1973). Phases are not given because they are meaningless unless a direction can be assigned to the EOFs. This has been done by Stacey et al. (1986) for the first mode at station 1.

ergy in the wind field, during the two observation periods, show that the wind was at least twice as energetic during the observation period being studied here. Therefore, it is perhaps not surprising that the wind had a greater influence on the currents.

The variability of the surface response from station to station, in the presence of such a large scale forcing mechanism, may have been caused by 1) the nonlinear character of the low-frequency currents, and 2) horizontal variations in the fresh surface layer, since any variations in the surface layer would obviously be reflected in the ability of the wind to transfer momentum to the bulk of the water column.

10. Longitudinal and transverse velocity correlations

The longitudinal and transverse velocity correlations, i.e.,

$$\overline{u_L(x)u_L(x+r)} \quad \text{and} \quad \overline{u_p(x)u_p(x+r)}$$

where $u_L(x)$ and $u_p(x)$ are the velocity fluctuations at x parallel and perpendicular to r (normalized to make the correlations equal to one when $r = 0$), allow a determination of the spatial scale of a flow. If they are functions only of $|r|$, i.e., if the flow is isotropic, and if the velocity field is horizontally nondivergent and homogeneous, then (Freeland and Gould, 1976)

$$g(r) = \frac{d}{dr} [rf(r)] \quad (2)$$

where $r = |r|$, and $f(r)$ and $g(r)$ represent the longitudinal and transverse correlation functions. By using (2) in the form

$$rf(r) = \int_0^r g(r) dr \quad (3)$$

one can make predictions of $f(r)$ from measurements of $g(r)$. If the predicted and measured $f(r)$ are the same, then the velocity field is consistent with horizontally nondivergent, isotropic flow, i.e., two dimensional isotropic turbulence. One can also fit analytical expressions of $f(r)$ and $g(r)$ that satisfy (2) to measurements of the longitudinal and transverse correlations. The better the fit, the more consistent the flow is with horizontal nondivergence and isotropy. For example, Freeland and Gould (1976) use the expressions

$$f(r) = (1 + br) \exp(-br) \quad (4)$$

$$g(r) = (1 + br - b^2 r^2) \exp(-br) \quad (5)$$

where $\phi = 1.618033 \dots$ is the golden ratio, R_c is the separation distance where $g(r) = 0$, and $b = \phi/R_c$. These are a one parameter set of functions that satisfy (2) and they are determined entirely by the choice made for the value of the parameter R_c .

Note that (4) gives us

$$\int_0^\infty f(r) dr = \frac{2R_c}{\phi} \approx 1.24R_c. \quad (6)$$

In this particular case the zero crossing in the transverse correlation function is similar in value to the integral under the curve of the longitudinal correlation function. This integral is a measure of the length scale of the fluctuations.

The longitudinal and transverse velocity correlations were calculated for each record pair at 100, 200 and 280/290 m. Because of the array design, measurements of the correlations were obtained at five discrete values of r . In Fig. 16 the averages and standard deviations are plotted as a function of separation distance for the three depths. The predicted values of $f(r)$, calculated from (3), are plotted as crosses. The integral in (3) was determined by drawing straight line segments between the measured values of $g(r)$ [and $g(0) \equiv 1$] and then determining the area under the curve. The curves (4) and (5) are shown as dotted lines.

At 100 m, $g(r)$ crosses zero at approximately 7.5 km. Also, the predicted and measured values of $f(r)$ are almost the same, and the analytical expressions match the data well. Thus the velocity field is consistent to a very close approximation with horizontally nondivergent, isotropic flow.

At 200 m, $g(r)$ crosses zero at approximately 5 km. In agreement with Yao et al. (1985), the spatial scale of the flow is decreasing with depth. The predicted values of $f(r)$ are less than the measured values, and the analytical expressions do not fit the data well. It appears that there are departures from horizontally nondivergent, isotropic flow. The flow is better correlated than (2) predicts.

At 280/290 m, $g(r)$ appears to cross zero at a separation slightly less than 5 km. Perhaps surprisingly, here the predicted values of $f(r)$ are closer to the measured values and the analytical expressions fit the data better than at 200 m. In fact, on average the flow appears to be relatively consistent with nondivergence and isotropy, even though, as previously discussed, there is a very coherent, tidally-forced flow at this depth. This coherence is reflected not in the mean values of $f(r)$, but in the standard deviations about the mean, which are much larger than at shallower depths. We do not know why this flow seems on average to satisfy the isotropy condition better than the flow at 200 m.

The short distances to the zero crossings in $g(r)$ (compared to the dominant frequencies of the currents) suggest that the flow is highly nonlinear and perhaps unstable. Correlations between the density and velocity fluctuations were found to be significant at zero lag at some locations and not at others. The best correlations were between U and σ_t fluctuations below 160 m at station 2; $\overline{U'\sigma_t'} \approx -0.5$ with 95% significance ≈ 0.35 . It is possible therefore that baroclinic instability moves

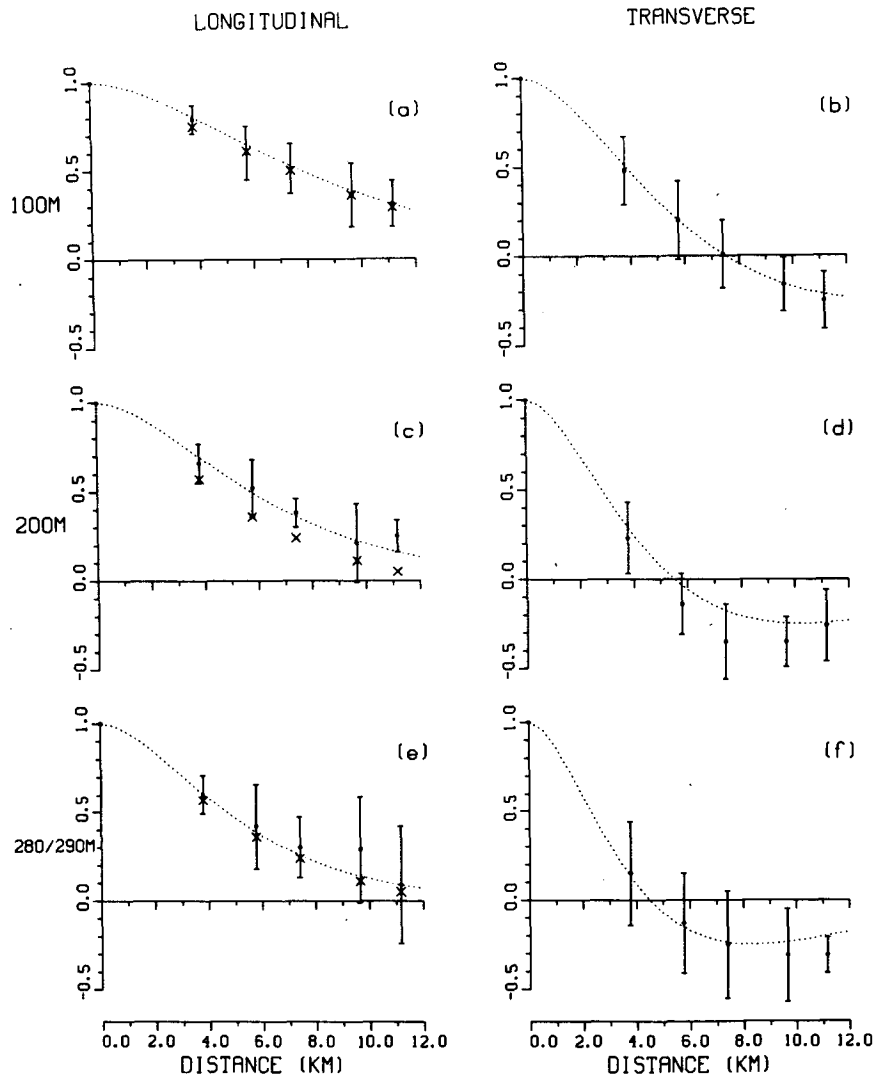


FIG. 16. Longitudinal and transverse correlations at 100, 200 and 280/290 m. The dots are the measured mean values and the error bars are the standard deviations. Going from the shortest to farthest separation distance the mean is the average of 9, 12, 6 and 3 independent estimates, respectively. The crosses are the longitudinal correlations as calculated from the measured mean values of the transverse correlation. The dotted lines are the longitudinal and transverse correlation functions as given by (4) and (5), with $R_c = 7.5, 5.5$ and 4.5 km at 100, 200 and 280/290 m, respectively.

energy to smaller scales. Consistent with the results of Yao et al. (1985), however, evidence for baroclinic instability is not always present, and so other instability mechanisms may be important too.

11. Summary and conclusions

It has been shown that wind stress at the surface, and the nonlinear interaction of the tides with topography at the bottom, probably forced much of the low-frequency motion in the Strait of Georgia from June 1984 until January 1985.

In the lower portion of the water column, the interaction of the tides with topography resulted in a primarily tidal, near-bottom response. It was coherent over the span of the experimental array, and had energy concentrated at the beat frequencies of the M_2, S_2 and N_2 tidal constituents. Significant tidal energy was also observed in shallower parts of the water column. Approximately one third of the low-frequency energy can be directly attributed to the tides.

Wind stress at the surface caused the formation of what appear to be Ekman spirals. At one cyclesonde station, the classical, constant eddy viscosity model of

an Ekman spiral fits the first-mode empirical orthogonal function very well down to a depth of 140 m. The orthogonal modes that dominate at depth differ qualitatively from the surface modes in that they tend to be more unidirectional where they dominate.

There is evidence that the wind and tidally forced motions interact nonlinearly. The empirical orthogonal functions that dominate the variance and resemble Ekman spirals near the surface, have significant peaks in their autospectra at tidal frequencies. Also, they are generally coherent with the modes that dominate at depth and have significant tidal energy.

Calculations of longitudinal and transverse velocity correlation functions show that at 100 m the current fluctuations were consistent with horizontally nondivergent, isotropic flow. At 200 m, the correlations deviated noticeably from nondivergence and isotropy. At 280/290 m, the flow was on average consistent with nondivergence and isotropy, but there were large variations about the mean.

The short zero crossings in the transverse correlations (<8 km) suggest that the low-frequency flow was highly nonlinear and perhaps unstable. There is evidence for baroclinic instability, but other instability mechanisms may have been important too.

Acknowledgments. This work is supported by the Natural Science and Engineering Research Council of Canada strategic grant A1108. We also thank the officers and crew of the CSS *Vector* and the technical staff of the Institute of Ocean Sciences for their assistance with the mooring work, and V. Lee for her assistance with the data analysis.

REFERENCES

- Chang, P., S. Pond and S. Tabata, 1976: Subsurface currents in the Strait of Georgia, west of Sturgeon Bank. *J. Fish. Res. Board Can.*, **33**, 2218–2241.
- Foreman, M. G. G., and R. F. Henry, 1979: Tidal analysis based on high and low water observations. *Pac. Mar. Sci. Rep.* **79-15**, 39 pp. Institute of Ocean Sciences, Sidney, B.C.
- Freeland, H. J., and W. J. Gould, 1976: Objective analysis of meso-scale ocean circulation features. *Deep-Sea Res.*, **23**, 915–923.
- Helbig, J. A., 1978: On the inertial instability of coastal flows. Ph.D. Thesis, University of British Columbia, Vancouver, 183 pp.
- , and L. A. Mysak, 1976: Strait of Georgia oscillations: low-frequency currents and topographic planetary waves. *J. Fish. Res. Board Can.*, **33**, 2329–2339.
- Kundu, P. K., and J. S. Allen, 1976: Some three-dimensional characteristics of low-frequency current fluctuations near the Oregon coast. *J. Phys. Oceanogr.*, **6**, 181–199.
- LeBlond, P. H., 1983: The Strait of Georgia: Functional anatomy of a coastal sea. *Can. J. Fish. Aquat. Sci.*, **40**, 1033–1063.
- Mooers, C. N. K., 1973: A technique for the cross spectrum analysis of pairs of complex-valued time series, with emphasis on properties of polarized components and rotational invariants. *Deep-Sea Res.*, **20**, 1129–1141.
- Pond, S., and G. L. Pickard, 1983: *Introductory Dynamical Oceanography*, Pergamon. 329 pp.
- Schott, F., and L. A. Mysak, 1980: On the structure of low-frequency current fluctuations in the Strait of Georgia. *Atmos.-Ocean*, **18**, 181–194.
- Schumacher, J. D., C. A. Pearson, R. L. Charnell and N. P. Laird, 1978: Regional response to forcing in southern Strait of Georgia. *Est. Coast. Mar. Sci.*, **7**, 79–91.
- Stacey, M. W., S. Pond and P. H. LeBlond, 1986: A wind-forced Ekman spiral as a good statistical fit to low-frequency currents in a coastal strait. *Science*, **233**, 470–472.
- Yao, T., S. Pond and L. A. Mysak, 1982: Low-frequency subsurface current and density fluctuations in the Strait of Georgia. *Atmos.-Ocean*, **20**, 340–356.
- , —, and —, 1985: Profiles of low-frequency subsurface current fluctuations in the Strait of Georgia during 1981 and 1982. *J. Geophys. Res.*, **90**, 7189–7198.